# Experimental Study of Falling Films by Simultaneous Laser-Induced Fluorescence, Particle Image Velocimetry and Particle Tracking Velocimetry

**Alexandros Charogiannis[1] and Christos N. Markides[1,*]**

1: Clean Energy Processes Laboratory, Department of Chemical Engineering,
Imperial College London, London SW7 2AZ, United Kingdom
* Correspondent author: c.markides@imperial.ac.uk

**Abstract** A measurement technique based on the simultaneous implementation of Laser-Induced Fluorescence (LIF), Particle Image Velocimetry (PIV) and Particle Tracking Velocimetry (PTV) has been applied to the study of wavy liquid falling film flows characterized by low Reynolds (*Re*) and Kapitza (*Ka*) numbers. The presently examined *Re* number range was 2.2 – 8.2, while the *Ka* number range was 28.6 – 41.4. The experimental methodology was developed with the ultimate aim of allowing for the evaluation of the local and instantaneous film thickness, interfacial velocity and velocity field from within the illuminated liquid volume underneath the wavy interface. The major challenges associated with the simultaneous implementation of the two optical diagnostic techniques were, firstly, the development of a refractive index correction approach allowing for liquids of different properties (surface tension and viscosity) to be tested, secondly, the identification of the location of the two liquid boundaries (solid-liquid and gas-liquid) in the LIF images, and lastly, the isolation of out-of-plane reflections from primary scattering regions in the raw PIV images. Following a detailed account of the novel practices formulated and utilized in tackling the aforementioned challenges, the efficacy of the proposed methodology is demonstrated through comparisons between laser-based measurements conducted in flat films, film thickness measurements performed with a micrometer, and the solution to the Navier-Stokes equation based on the assumptions of one-dimensional (1-D), steady and fully developed flow. In addition, sample film topology results are presented for a range of flow pulsation frequencies (1 – 8 Hz), while film thickness and interfacial velocity time traces were reconstructed and are presented along with film thickness and interfacial velocity statistical results for select flow conditions.

## 1. Introduction

Liquid film flows are encountered in a wide range of industrial processes such as wetted-wall absorbers, condensers, evaporators and reactors, owing to their high surface-to-volume ratios and associated heat and mass transfer capabilities even at modest flow rates. Extended theoretical and experimental investigations suggest that the rates of heat and mass transfer are strongly linked to the spatiotemporal variations of the hydrodynamic characteristics of these films, and in particular the waviness of the gas-liquid interface (Brauner and Maron 1982, Mudawar and Houpt 1993, Alekseenko, Nakoryakov et al. 1996). Commonly employed geometries involve liquid films falling down vertical or inclined flat plates and annular or square cross-section tubes, with flow visualization experiments aimed at uncovering the two-phase flow mechanisms behind the development and interaction of interfacial instabilities, as well as at providing validation data for analytical models and numerical simulations. Despite the numerous flow visualization studies encountered in literature, only a limited number of publications relating to the spatiotemporal variations of film thickness and velocity are currently available; an observation inherently linked to the restricted nature of the liquid domains under observation (often sub-millimetric) and the intermittent nature of the moving and curved interface, which render the extraction of relevant information particularly challenging. The present study is motivated by the demand for simultaneous, time-resolved film thickness and velocity data from within film structures in falling film flows.

Optical diagnostics have been extensively applied to the study of liquid and gaseous flows, as they allow for non-invasive real-time imaging and interpretation of one, two or three-dimensional spatial distributions of seeded or naturally occurring tracers or particles. Regarding the investigation of unsteady interfacial flows, and in particular the instantaneous motion of liquid films, a range of optical methods have been attempted. Typically a molecular tagging approach is employed, whereby small quantities of fluorescing dyes are dissolved in an optically transparent liquid. Following irradiation, for example by a laser source, a

red-shifted emission (fluorescence) is observed; collection of the fluorescence signal by a detector, for example a CCD (charged coupled device) camera, subsequently allows for visualization of the illuminated region of the flow. The photochromic dye activation (PDA) technique, which has been used to examine the hydrodynamic structure of liquid films over a wide range of flow regimes (Karimi and Kawaji 1998, Kawaji 1998, Moran, Inumaru et al. 2002), stands for a prime example of the particular approach. In this case, thin traces arranged in a grid pattern perpendicular to the direction of the flow serve as local markers of the gas-liquid interface and wall-liquid boundary, while the displacement of the grid points can be used to obtain velocity profiles. Alternatively, uniform illumination of the investigated flow field can be used to resolve the spatiotemporal film thickness variation over a two-dimensional region by deployment of Laser Induced Fluorescence (LIF) imaging. Biacetyl LIF (Schagen, Modigell et al. 2006), for example, has been employed in the investigation of film thickness instabilities developing over the surface of a vertically falling heated film, while Rhodamine B LIF imaging has been used to study the spatiotemporal film thickness variation over an inclined heated plate (Mathie , Nakamura et al. 2013), as well as in gas-liquid annular flows (Schubring, Ashwood et al. 2010, Zadrazil, Matar et al. 2014). Finally, Rhodamine 6G LIF visualization has been utilized over a wide range of flow conditions emerging in downwards annular flows (Alekseenko, Antipin et al. 2009, Alekseenko, Cherdantsev et al. 2012). Examples of instantaneous film thickness measurements of wavy thin films seeded with a fluorescing dye by back-illumination are also commonplace (Liu and Gollub 1993, Liu and Gollub 1994).

Aside from molecular tagging, instantaneous velocity measurements can be obtained by Laser Doppler Velocimetry (LDV) (Mudawar and Houpt 1993), Particle Image Velocimetry (PIV) and Particle Tracking Velocimetry (PTV) (Schubring, Foster et al. 2009). LDV offers point measurements only, whereas the deployment of PIV/PTV permits two-dimensional velocity vector maps to be generated. These techniques are based on tracking the motion of seeded particle groups (PIV) or individual particles (PTV), by sequential illumination and image acquisition within a small interframe duration. The obtained imaged pairs are then processed by typically using a cross-correlation, multi-pass approach. Selection between the two techniques is typically based on resolution requirements, with PTV offering superior resolution, albeit at the cost of increased processing time

In the present study, the spatiotemporal variations of the film thickness (liquid depth) and interfacial velocity of isothermal liquid films developing over the surface of an inclined flat glass plate are studied by simultaneous employment of Rhodamine B LIF and PIV/PTV. The primary objective of this contribution is to establish the methodology behind the combined optical technique, and present exemplary study cases that demonstrate its application. The latter will be limited, at present, to low Reynolds ($Re$) numbers, in the 2.2 – 8.2 range, and low Kapitza ($Ka$) numbers, in the 28.6 – 41.4 range. In the future, however, simultaneous LIF and PIV/PTV will be employed in the study of the dynamics of falling films spanning a wide range of both $Re$ and $Ka$ numbers.

Following a description of the arrangement employed in these experiments, a detailed account of the experimental methodology developed with the ultimate goal of simultaneously conducting LIF and PIV/PTV measurements will be provided. Finally, the efficacy of this methodology will be demonstrated by presenting comparative measurements and select film topology and statistical results. Prior to commencing with the introduction of the experimental setup, it is essential to establish the definitions of the two aforementioned dimensionless numbers that stand for the principal experimental parameters of this study. The $Re$ number provides a quantitative expression for the relative significance between inertial and viscous forces, and is defined in terms of a characteristic flow velocity $U$, dimension $D$ and the kinematic viscosity of the fluid $\nu_f$:

$$Re = \frac{UD}{\nu_f} \tag{1}$$

The Kapitza number expresses the dimensionless ratio between surface tension and inertial forces, and acts as an indicator of the hydrodynamic wave regime. In the expression provided below (Equation 2), $\sigma_f$ stands for the liquid surface tension, $\rho_f$ is liquid density, $\theta$ is inclination angle, and $g$ is gravitational acceleration:

$$Ka = \frac{\sigma_f}{\rho \nu_f^{4/3} \sin(\theta) g^{1/3}} \tag{2}$$

## 2. Experimental Setup

### 2.1 Flow Loop

A schematic representation of the experimental configuration, itself an evolution of a previously employed setup (Markides and Mathie 2013, Markides and Mathie 2013, Mathie , Nakamura and Markides 2013), is presented in Figure 1. The setup consists of a test section, over which wavy film flows develop, and a closed loop, via which the liquid circulates. A closed as opposed to an open loop was selected so that the fluorescent dye and PIV particle concentrations remain constant throughout the imaging experiments. The tank located underneath the test section acts as a temporary reservoir for the liquid flowing round the loop, while when not in operation, it assumes the role of a storage reservoir. When in operation, the flow is passed through a counter flow heat exchanger purchased from Alfa Laval, in order extract the heat imparted on the fluid due to pumping work On account of the relatively high viscosity of the presently employed aqueous glycerol solution (the properties of which will be provided in section 3.3) and despite the fact that no heating (such electrical heating at the test section) was purposefully provided to the liquid film, the temperature of the fluid rises from around 25 °C to 30 °C within a few minutes of operation even at intermediate flow rates. Consequently, the employment of a cooling system was rendered essential. The heat exchanger cooling line was fed by the water mains, whilst the rate of heat extraction was modulated by adjusting the water flow rate (valve V3 in Figure 1). It was later found by monitoring the temperature inside the distribution box that the local liquid temperature could be maintained to within 0.5 °C by employment of the particular tactic over the course of an experimental run. Valves V1 and V2 were used to isolate the pump (Grundfos CHI 4-30) from the rest of the loop when, for example, replacing the liquid mixture, while valve V4 was responsible for bypassing part of the flow back to the tank. In that way, a higher flow rate could be maintained through the pump than the one intended for the experiment, effectively reducing the likelihood of stalling and cavitation, and allowing for more efficient operation of the heat exchanger and therefore more accurate control of the liquid temperature. The pump rotational speed was controlled using a 1200 VA variable autotransformer (Carroll & Meynell).

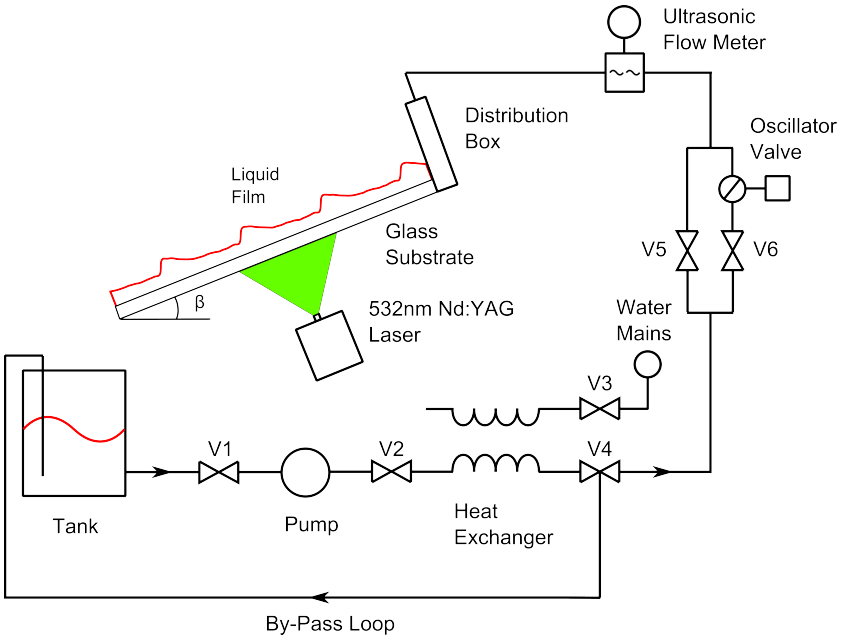


**Fig. 1** Schematic representation of the liquid flow loop comprised of the test section (glass plate over which film flows develop), a pump used to circulate the liquid, a heat exchanger installed in order to modulate the liquid temperature, an oscillator valve used to instigate the formation of waves at select frequencies, and finally a bypass loop.

Past the bypass valve, the flow was split to form two separate supplies; a steady and a pulsating supply. The pulsating supply was generated by diverting a portion of the total flow through an oscillator valve. The oscillator valve comprises a metallic spindle with a hole drilled transversely through it (throttle), rotating within the valve body. Torque was provided to the throttle by a 5 V, 1 A, 1.8 ° step angle stepper motor

controlled by an in-house developed stepper motor controller. The TTL pulse output of a TTI TG315 function generator was used to regulate the oscillator valve rotational speed, achieving a maximum of approximately 370 rpm (corresponding to a wave frequency of slightly above 11 Hz). Past the oscillator valve, the two supplies recombine prior to entering the distribution box. The reason for employing this setup is to achieve better control over the wave frequency and amplitude, selectively triggering the rapid growth of regular waves and fully developed wave regimes within the confines of a short test section.

A final component installed on the flow loop was an ultrasonic flow meter (UF25B by Cynergy3 Components). The particular component operates by measuring the transit time between ultrasonic pulses propagating along and against the direction of the flow, and generates an electronic pulse for every milliliter of flow that passes through it. The flowmeter output was recorded by a National Instruments data acquisition card (NI USB-6211) operated using MatLab and triggered by output TTL pulses generated by the laser. The recorded pulse sequences were then used to reconstruct the instantaneous flow rate and cumulative flow volume time traces, from which the mean flow rate and intensity of pulsation were calculated (Figure 2).

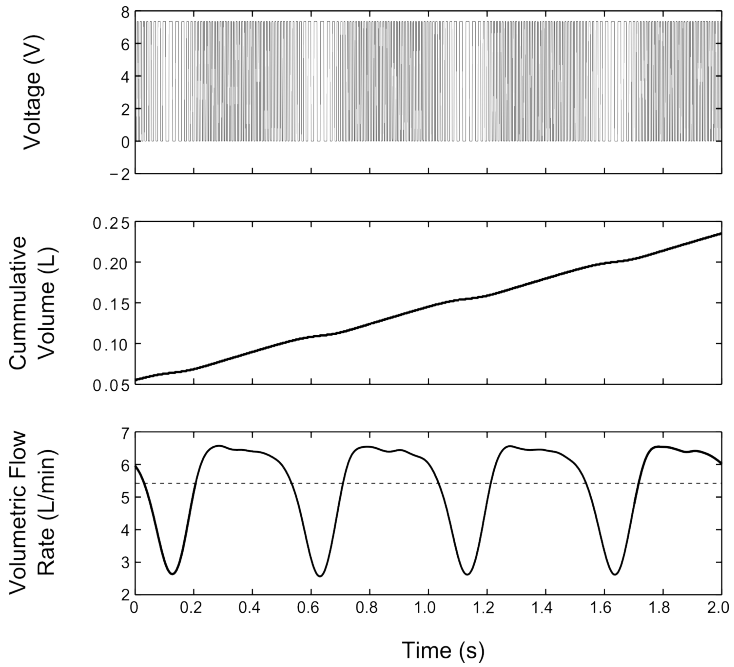


**Fig. 2** Instantaneous flowmeter output signal (top), instantaneous cumulative liquid volume passing through the flowmeter in L (middle), and instantaneous volumetric flow rate in L/min (bottom).

The average flow rate can be calculated by either dividing the total liquid volume by the sampling time, or by averaging out the instantaneous flow rate; both approaches return the same result. The peak amplitude of pulsation is estimated as one half of the average disparity between local flow rate maxima and minima, while the intensity of pulsation is obtained by dividing the peak amplitude by the mean flow rate.

### 2.2 Test Section

The test section comprises a 400 × 300 mm soda lime glass plate of 0.7 mm thickness (Instrument Glasses) and is mounted on an aluminum support frame. Support to the glass is provided along its periphery in order to maximize the optically accessible area. Hinges installed on either side of the frame allow for adjustment of the test section inclination angle, presently set to 20 °. The particular experimental parameter is of outmost importance when investigating the dynamics of film flows; however, as the objective of the present study is to establish a combined LIF and PIV/PTV optical imaging methodology, and examine the effects of the *Re* and *Ka* numbers, as well as that of pulsation frequency on isothermal film flow dynamics, the inclination angle was not varied. A flow distribution box acting as a settling chamber and comprised of meshes and a honeycomb was installed at the top of the test section in order to uniformly dispense the flow across the span of the plate, as well as to break down and dissipate any large scale eddies and turbulence. The outlet of the chamber is equipped with a knife edge, the height of which can be adjusted by a pair of micrometer stages in

order to regulate the flow contraction and prevent the generation of a hydraulic jump or air flow back into the box. Prior to each experimental run, the distribution box was manually primed using a syringe, while a type-K thermocouple was installed allowing for the liquid temperature to be monitored. A calibrated Omega microprocessor thermometer was employed in reading off liquid temperature values. Using the mean flow rate measurement from the ultrasonic flowmeter, an *Re* number can be defined for the flow inside the distribution box (Equation 3):

$$Re = \frac{DU_{\mathrm{box}}}{\nu_{\mathrm{f}}} = \frac{\Gamma}{\nu_{\mathrm{f}}} \tag{3}$$

In the above expression, $U_{\mathrm{box}}$ stands for the velocity inside the distribution box, $D$ is the channel depth (20 mm) and $\Gamma$ is the flow rate per unit width of the channel (300 mm).

As can be observed by inspection of Figure 1, excitation of the dye-doped liquid flowing down the inclined glass plate was performed from the solid-liquid interface side rather than the free film surface. The benefits of adopting the particular arrangement are instrumental with regards to the successful realization of the proposed combined LIF and PIV/PTV diagnostic strategy. If, instead, the moving wavy free surface was illuminated, the laser sheet would be subjected to strong, spatially and temporally non-uniform beam stirring and lensing. In addition to illumination, imaging was also carried out from underneath the test section (Figure 2); an arrangement that was preferred in order to limit the presence of out-of-plane reflections within the field of view of the collection optics.

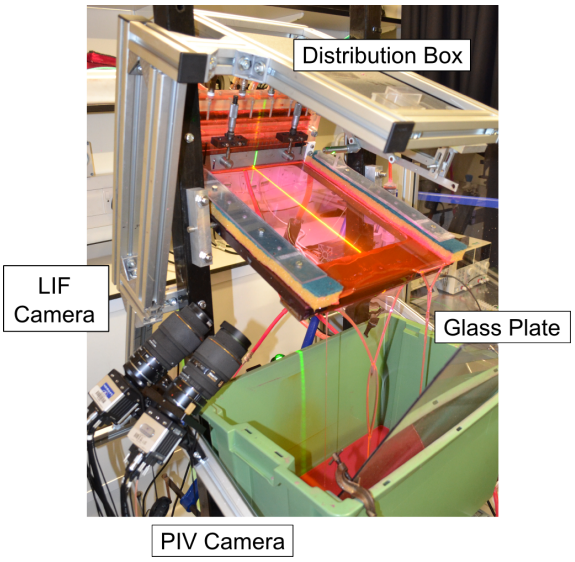


**Fig. 3** Test section arrangement showing the position of the laser sheet optics, camera and illuminated region of the film falling down the inclined glass plate.

### 2.3 Laser and Imaging Setup

For the purposes of this experiment, a double-cavity frequency-doubled Nd:YAG laser (Nano-L-50-100PV by Litron Lasers) was used to excite the Rhodamine B seeded liquid at a rate of 100 Hz. The maximum available laser energy at 532 nm, the second harmonic of the laser, is approximately 50 mJ/pulse. Sheet optics with a 10 ° divergence are employed in forming a thin (approximately 200 μm) sheet extending over the length of the glass plate. The collection optics are comprised of a pair of LaVision VC-Imager Pro HS 500 CMOS cameras equipped with Sigma 105 mm f/2.8 Macro lenses. Extension rings (32 mm) were installed on both cameras in order to achieve the desired magnification (imaging region along the film corresponds to approximately 33 mm), while a Scheimpflug adaptor was installed on the PIV camera. The latter was positioned at a slight angle relative to the imaging plane, and consequently, part of the imaging region along the direction of the flow would be out of focus. Both cameras and lasers were synchronized by a LaVision High Speed Controller (HSC), operated using the LaVision Davis 8.2.0 software.

A particularly challenging aspect of optical diagnostics in film flows is correcting for optical distortions stemming from the refractive index mismatch between the liquid and transparent solid responsible for

containing the flow and allowing for optical access (Budwig 1994). In addition, optical distortions often arise on account of geometrical restrictions associated with the solid domain; for example, in the case of annular flows, no solid surface parallel to the imaging plane is available (Zadrazil, Matar and Markides 2014). It has, therefore, become common practice to employ a "correction box", a transparent component either solid or hollow and filled with a transparent liquid, in order to *a priori* account for both aforementioned distortion sources. Clearly, the utmost advantage of the particular approach is that despite the correction performed, the imaging system resolution is preserved, while its greatest shortcoming is the resulting refractive index restriction imposed on fluid selection. In other words, the liquid component is selected on the basis of matching the refractive index of the correction box material, rather than based on its flow related properties (such as the viscosity and surface tension). For the purposes of the presented experiments for which the variation of the *Ka* number by tailoring the viscosity, surface tension and density of the liquid is a primary objective, the implementation of an alternative approach was necessary: In order to perform simultaneous LIF and PIV/PTV measurements, the imaging planes of both cameras were mapped and corrected for perspective distortions using a calibration graticule immersed inside the employed liquid mixture. For this purpose, a Perspex box with its bottom surface removed (the surface that would otherwise adhere to the glass plate) was carefully positioned and held at the imaging plane, and subsequently filled with the liquid mixture through a hole at its top surface using a syringe. In that way, accurate scaling of LIF/PIV imaging domain could be performed for any selected liquid composition. Calibration graticule images obtained through practical implementation of the above-described procedure are presented in Figure 4.

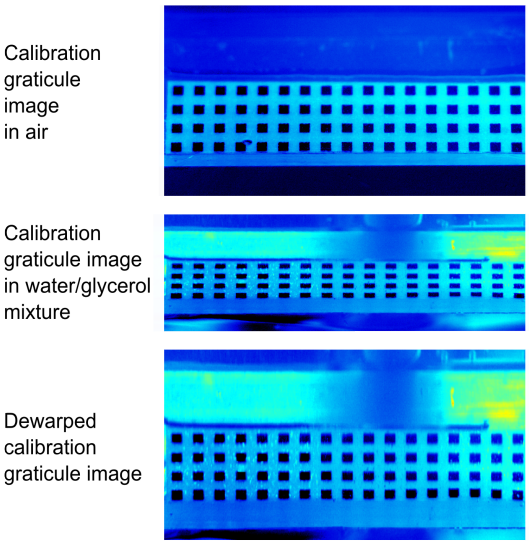


**Fig. 4** Calibration graticule image in air (top), in aqueous glycerol solution (middle) and in aqueous glycerol solution following refractive and perspective distortion corrections.

Mapping and optical distortion corrections for the two-camera setup were performed using a pinhole model available in Davis, with the resulting apparent resolution being 29.7 μm/pixel, and root mean square error of the fit being approximately 0.5 pixels. Another key aspect relevant to the simultaneous implementation of LIF and PIV/PTV imaging was the appropriate camera filter selection, and in particular, the filter of the PIV camera. PIV is performed by imaging the light scattered off the surfaces of particles seeded in the flow; in order to block any red-shifted fluorescence light, band-pass filters allowing only a narrow spectral region (typically 5 – 10 nm) to be imaged are typically employed. The adoption, however, of such a filter prevented the two-camera mapping procedure to be performed as no sufficient light could be collected without laser illumination. Instead, a short-pass filter (Edmund Optics, part number 84-721) with a cut-off frequency at 550 nm was employed, making the entire visible spectrum below 550 nm accessible for camera calibration purposes. The downside associated with the utilization of the particular component is that part of the Rhodamine fluorescence signal is present in the PIV images as a consequence of the spectral overlap between the absorption and emission spectra of the seeded tracer (section 3.2 PIV Image Processing). For the purposes of LIF imaging, a long-pass optical filter purchased from LaVision (cut-off frequency at 540 nm) was utilized instead. The dye (Rhodamine B purchased from Sigma-Aldrich)

concentration was approximately 0.5 g/L, while glass hollow spheres (LaVision, 11.7 μm mean diameter) were seeded at a concentration of approximately 0.18 g/l for tracking the fluid motion.

## 3. Experimental Methodology

### 3.1 LIF Data Acquisition and Processing

The LIF camera was operated in dual frame mode (like the PIV camera), so that for every PIV frame, a corresponding LIF frame was acquired. The interframe separation D*t* between two successive frames (in reference to double frame acquisition mode) was set to 1.5 ms, corresponding to a fluid displacement at the interface of around 8 – 15 pixels. Each experimental run was comprised of 1000 LIF image pairs collected successively with a frequency of 100 Hz. A sample LIF image, along with its processed and binarized counterparts is presented below (Figure 5).

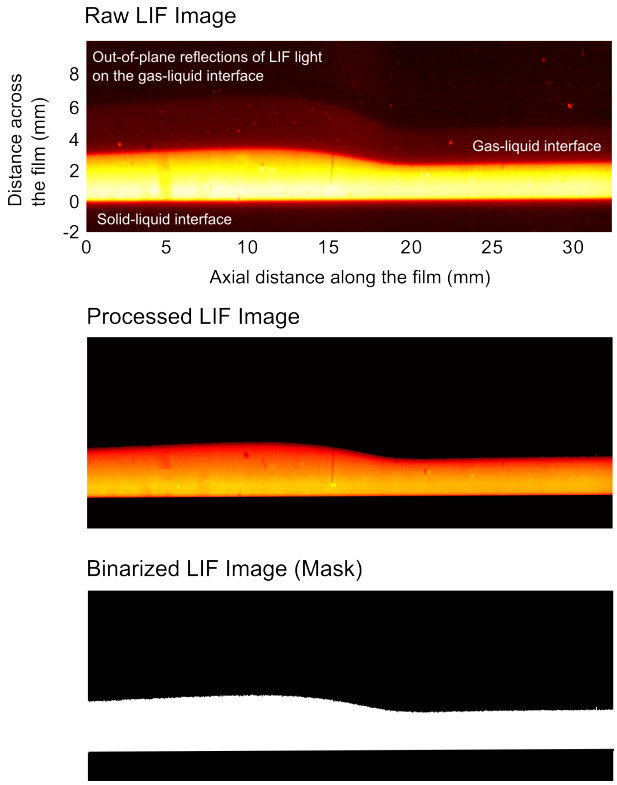


**Fig. 5** Refractive index and perspective distortion corrected LIF image (top), processed LIF image in MatLab whereby the solid-liquid and gas-liquid interfaces have been located and out-of-plane reflections have been removed (middle), and binarized LIF image produced to mask out the liquid domain in the corresponding PIV image.

The first frame from top in Figure 5 shows a film fluorescence image corrected for perspective distortion in Davis. Close inspection of the apparent solid-liquid and gas-liquid boundaries reveals the presence of reflections; in the case of the solid-liquid interface, secondary reflections originating from the glass surface in contact with the liquid blur the LIF signal locally, while with regards to the gas-liquid interface, the fluorescence emitted by the illuminated liquid volume is reflected from the interface back to the camera. Moreover, the reflection intensity above and ahead of the wave appears to be higher compared to the rest of the image; an effect most probably attributed to the curvature of the interface at the particular location and manifested by lensing of the LIF light emitted by the liquid bulk.

In systematically identifying the location of the two interfaces, different methods where devised and examined using an in-house developed MatLab processing routine. The location of the solid-liquid interface, for example, can be derived directly from the calibration performed with the graticule. This approach, however, assumes that the graticule attached to the calibration box is perfectly aligned with the solid-liquid boundary; if it is not, a systematic error will ensue despite the fact that the image might be scaled correctly. Alternatively, the LIF signal can be used to obtain the location of the solid-liquid boundary, a tactic presently

adopted through the implementation of an edge detection algorithm. The particular processing routine is typically employed in obtaining the Step Response Function (SRF) of an imaging system by use of the scanning edge technique (Zhu, Kaftandjian et al. 1995), while in addition to edge location identification, also provides the edge inclination. In our case, this serves as an assessment of the distortion correction efficacy; the presence of a non-zero edge inclination angle being a direct consequence of misalignment between the calibration graticule and solid substrate.

With respect to the gas-liquid interface identification, an intensity threshold and two gradient methods were considered, and are pictorially presented in Figure 6.

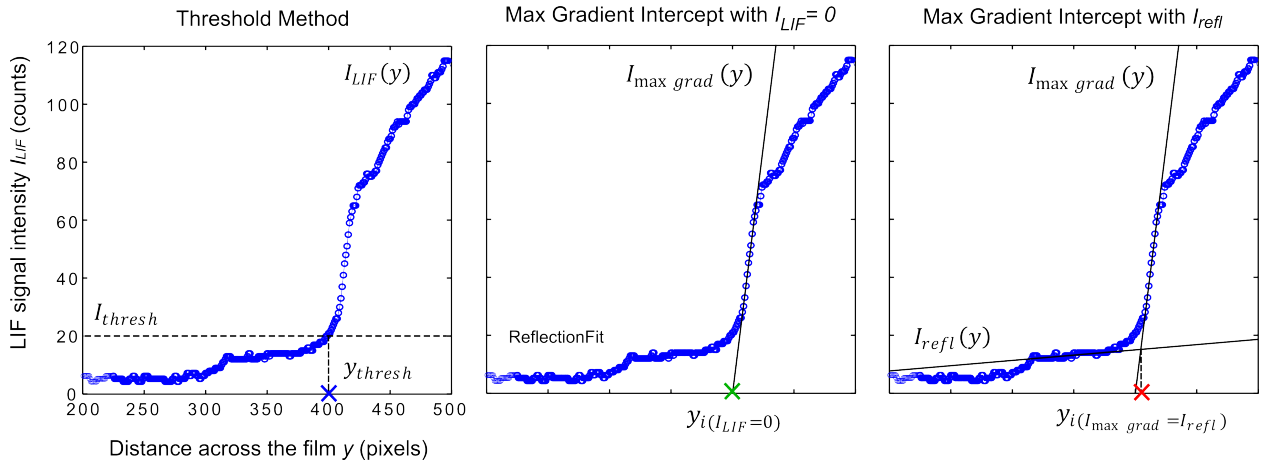


**Fig. 6** LIF intensity profile across the liquid domain indicating the intensity threshold methodology for locating the gas-liquid interface (left) and maximum gradient intercept with the $I_{\mathrm{LIF}} = 0$ line and reflection first order polynomial fit.

In the first case, an estimate of the position of the interface $y_{thresh}$ is obtained on a per column basis by setting a threshold intensity value $I_{thresh}$ corresponding to a percentage of the maximum LIF signal:

$$y_{\mathrm{thresh}} = \arg_y(I_{\mathrm{LIF}}(y) - I_{\mathrm{thresh}} = 0) \tag{4}$$

This tactic takes into consideration the fact that the reflection intensity scales with the signal intensity; however, it fails to account for local lensing effects and consequently overestimates the film thickness where the interface is strongly curved. The maximum (negative) gradient approach estimates the location of the interface $y_{i(I_{\mathrm{LIF}}=0)}$ as the intercept of the maximum gradient line and the zero signal intensity axis:

$$y_{i(I_{\mathrm{LIF}}=0)} = y_{\mathrm{max,grad}}\left(1 + \frac{I_{\mathrm{LIF}}(y_{\mathrm{max-grad}})}{\left(\frac{\partial I_{\mathrm{LIF}}}{\partial y}(y_{\mathrm{max-grad}})\right)}\right) \tag{5}$$

Where $y_{max\ grad}$ is the $y$ coordinate of the location of the maximum negative gradient:

$$y_{\mathrm{max,grad}} = \arg_y\left(\max\left(-\frac{\partial I_{LIF}}{\partial y}\right)\right) \tag{6}$$

This approach, presented in the middle plot of Figure 6, was found to be more robust that the threshold method as it remains largely unaffected by locally higher reflection intensities. Finally, a methodology incorporating elements from the other two was developed, whereby the location of the interface $y_{i(I_{\mathrm{max,grad}}=I_{\mathrm{refl}})}$ is estimated as the intercept between the maximum LIF signal gradient line $I_{\mathrm{max,grad}}(y)$, and a line derived by fitting a first order polynomial to the reflection intensity profile $I_{\mathrm{refl}}(y)$. In more detail, starting off from the peak LIF signal intensity per column, the purely reflection signal onset is taken as the first non-negative gradient location. The signal intensities of the next 20 pixels are then stored, averaged on a

per image basis, and employed in producing the reflection line:

$$y_{i(I_{\max,\text{gead}}=I_{\text{refl}})} = \arg_y\left(I_{\max,\text{grad}}(y) - I_{\text{refl}}(y) = 0\right) \quad (7)$$

Along with this practice, the collected reflection data points are also averaged on a per column basis providing an indication of the refection intensity profile along each image, with a local spike typically identified in regions where the wavy interface causes lensing. Compared to the maximum gradient method, the reflection intercept method produced smoother film thickness results, while the gas-liquid interface location estimates were always closer to the initial signal increase which is believed to be a more accurate estimate of the gas-liquid interface position. The effectiveness of the last method, in conjunction with the solid-liquid interface location approach in estimating the film thickness, is examined in Section 4.1.

Sample film thickness profiles extracted from successive LIF images using the third interface identification approach are displayed in Figure 7. As a final processing step, the thickness traces were subjected to 3x3 median filtering in order to minimize the signal noise while preserving the signal features. The processed thickness profiles were then used to mask out the LIF image regions not corresponding to film fluorescence, such as the reflection regions (middle frame in Figure 5), and produce binarized images (lower frame in Figure 5) where signal intensity of 1 corresponds to the liquid film region and signal intensity of 0 is ascribed to the rest of the imaging region. The binarized LIF images were subsequently employed in correcting their respective PIV images for out-of-plane reflections (Section 3.2)

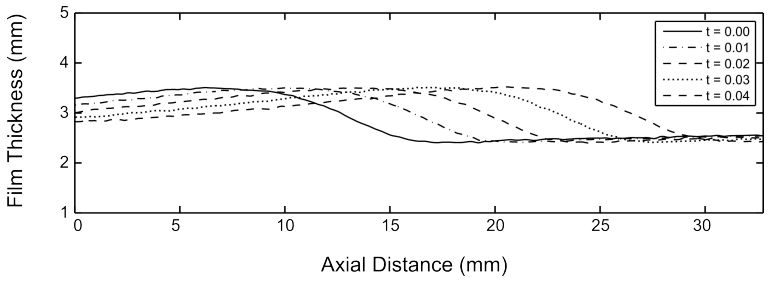


**Fig. 7** Film thickness profiles of a wave propagating along the direction of the flow extracted from successive LIF images.

### 3.2 PIV Data Acquisition and Processing

As was discussed earlier (Section 3.1), raw image pairs were collected with the PIV camera with an interframe time delay of 1.5 ms; a sample refractive index and perspective distortion corrected raw PIV image is displayed at the top frame of Figure 8. In addition to the laser light scattered off the particle surfaces and background fluorescence signal from the liquid phase, two artefacts are also clearly discernible: First, a reflection from the lower glass surface, and second, a reflection of the particle scattering signal of the entire illuminated volume emanating from the gas-liquid interface. It should be noted that similar to the reflection observed atop of the liquid film in the fluorescence images, this reflection also trails the waviness of the gas-liquid interface. In contrast to the fluorescence signal reflection, however, the intensity of the reflected scattering signal is comparable to the original signal, rendering the identification of secondary scattering signals from the PIV images alone highly non-trivial.

In order to examine the particular effect and demonstrate that the particle scattering signal is indeed reflected about the interface, particle imaging experiments were conducted using Rhodamine B doped PIV particles (LaVision, 10 μm mean diameter). The reason for selecting the specific particles for the purposes of this experiment is that they can be imaged with both LIF and PIV cameras, as part of the incident laser light is absorbed and re-emitted as red-shifted fluorescence, and part of it is scattered. Sample LIF and PIV images of a particle pair collected successively at 0.02 s intervals, and corresponding to these imaging experiments, are shown in Figure 9. Particle 1 is located very near the interface, while Particle 2 is suspended approximately halfway across the film height and further downstream along the direction of the flow (LIF frame at $t$ = 0.00 s). The same particle pair imaged simultaneously with the PIV camera appears twice, with Particle 1 observed as a double particle and Particle 2 mirrored about the interface. The next two LIF/PIV frames capture the same particle pair at $t$ = 0.02 s and $t$ = 0.04 s, with Particle 1 overtaking Particle

2 along the direction of the flow as a result of the higher velocity at the interface compared to the liquid bulk (parabolic velocity profile).

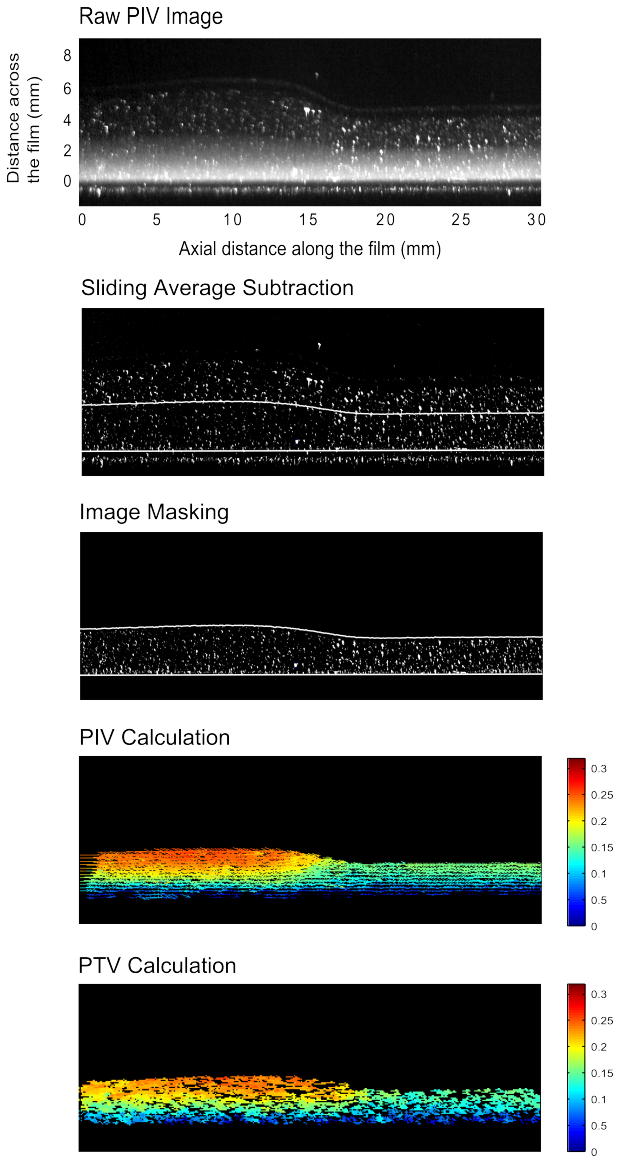


**Fig. 8** Refractive index and perspective distortion corrected PIV image (top), the same image following 3×3 sliding average subtraction (second from top), masked particle image using its processed LIF counterpart (middle), PIV velocity vector map obtained from a masked image pair such as the one shown above (second from bottom), PTV velocity vector map obtained following the PIV calculation.

Returning to the PIV image acquisition and processing, once a 1000 double frame run is completed, the sequence of collected image pairs is evaluated using the Davis PIV/PTV algorithms. Following corrections for refractive index and perspective distortion, the collected particle image pairs were preprocessed (3 × 3 sliding average subtraction) in order to eliminate the liquid fluorescence background (second frame from top, Figure 8). The binarized images generated by the LIF image processing routine in MatLab were then imported in Davis and employed in masking out the image regions associated with reflections from both the substrate and gas-liquid interface (third frame from top, Figure 8). The masking procedure was carried out by the Davis PIV/PTV algorithm, with vectors calculated only for pixels inside the masked area, and vectors disabled if the ratio of masked out to all pixels from within the interrogation window was higher than 0.2 for the first pass, and 0.5 for all other passes. Finally, the masked particle images were used to generate two-dimensional (2-D) velocity vector maps using a four-pass cross-correlation approach. During the first and second passes (initial velocity field estimation), a 32 × 32 pixel interrogation window was selected with the

overlap parameter set to 50%. During the third and fourth passes, the interrogation window was reduced to 16 × 16 pixels with 50% overlap. Spurious vectors (vectors having a norm or direction significantly disparate compared to their neighbors) were removed during vector post-processing by applying allowable vector range restrictions and median filtering. The vector-to-vector spatial resolution was 238 μm. PTV velocity vector maps were subsequently calculated by employment of the obtained PIV results, an 8-pixel correlation window size, and a 1 – 3 pixel particle size range (bottom frame, Figure 8). The latter was implemented in order to account for the effects of dewarping and collection optics point spread function on the apparent image size of the particles.

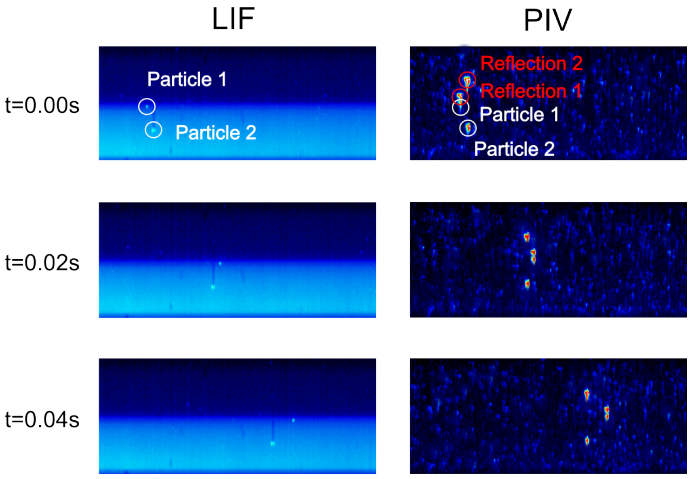


**Fig. 9** Rhodamine B particle pair imaged at three successive time instances using two cameras; one equipped with a long-pass LIF filter and one equipped with a band-pass PIV filter. In the case of the PIV imaging setup, the particle pair is observed twice; once as a real image corresponding to the one observed with the LIF setup, and then as a mirror image due to reflection about the interface.

Once the PIV and PTV velocity vector maps have been produced, instantaneous velocity profiles from within the wavy films can be constructed (see for example Figure 10). The hereby presented velocity profiles were calculated by spatially averaging PIV and PTV data over manually selected 2.4 mm regions along the stream wise direction of the flow (corresponding to a maximum of 10 PIV vectors). The displayed film thickness profile was obtained from the LIF processing routine as described in the previous subsection. What becomes instantly apparent is the strikingly superior resolution of the PTV compared to the PIV calculation, albeit at the expense of increased processing time and storage capacity requirements.

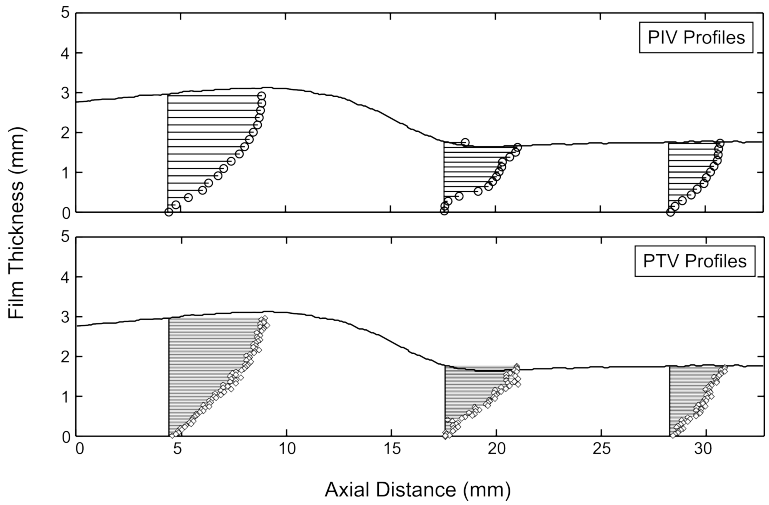


**Fig. 10** Instantaneous velocity profiles, produced by spatially averaging PIV (top plot) and PTV (bottom plot) velocity data, superimposed on the corresponding instantaneous film thickness profile, the latter extracted from an LIF image.

### 3.3 Fluid property measurements

The surface tension and viscosity of the aqueous glycerol solution employed in these experiments (approximately 81% glycerol by weight), were determined experimentally. First, an Attension Sigma 700 force tensiometer with a Wilhelmy plate was used to quantify the surface tension of samples collected throughout the duration of optical measurement runs. Once a sample was placed in the tensiometer, it was heated to the desired temperature before surface tension measurements were conducted. For the viscosity measurements, a Poulten Selfe & Lee U-tube viscometer was employed. Initially, the viscometer was placed inside a water bath in order to stabilize the temperature of the sample to the desired level; once the desired temperature was attained, the time required for the liquid sample to flow through two marked positions above and below the upper bulb of the viscometer tube was measured. This time correlates to the kinematic viscosity $\nu_f$ of the sample according to the following expression:

$$\nu_f = \left[\frac{mm^2}{s}\right] = C\left[\frac{mm^2}{s^2}\right] * t[s] \quad (8)$$

The constant $C$ is provided by the viscometer supplier and applies to the particular viscometer type only ($C$ = 0.09530 mm$^2$/s). Both surface tension and viscosity measurements were conducted for three different fluid temperatures corresponding to the experimental measurements. The obtained results, later used to calculate the flow *Re* and *Ka* numbers, are tabulated below (Table 1). The quoted uncertainties correspond to the mean difference between the maximum and minimum values observed amongst five independent measurements (five different samples) for each condition (temperature). It should finally be noted that no systematic variation was observed in the surface tension measurements between samples collected throughout the duration of the thin film experiments; a prospect ensuing from the presence of surfactants in laboratory environments such as dust and particles.

**Table 1.** Experimentally determined kinematic viscosity and surface tension values of the aqueous glycerol solutions employed in the present experiments at three different temperatures; 25 °C, 28 °C and 30 °C

| | Temperature (°C) | | |
|---|---|---|---|
| | 25.0±0.1 | 28.0±0.1 | 30.0±0.1 |
| Kinematic Viscosity (mm$^2$/s) | 61.7 ± 0.7 | 51.4 ± 1.2 | 46.0 ± 1.0 |
| Surface Tension (mN/m) | 62.3 ± 0.5 | 61.8 ± 0.3 | 60.6 ± 0.2 |

Finally, the density of the aqueous glycerol solution (1214 ± 2 kg/m$^3$) was measured using an electronic scale and 1 liter beaker. The measurement was repeated five times and the quoted uncertainty was calculated in the same manner as for the surface tension and viscosity measurements.

## 4. Results and Discussion

### 4.1 Validation Experiments

Film thickness measurements using the proposed LIF imaging setup were carried out for flat (unpulsed) films and were compared to measurements carried out using a micrometer (10 μm smallest scale division). The objective of the particular experiment was to obtain independent film thickness data allowing for the identification of potential systematic errors in the LIF measurement tactic. Initially, images of the dotted target immersed in the glycerol/water mixture were collected and averaged, and an image calibration (optical distortion correction) was performed in the same manner as discussed earlier. Next, a micrometer was set up on top of the imaging region and a reading of the wall location was obtained. Films of different thicknesses where generated by varying the power input to the pump and adjusting the portion of the flow bypassing the test section (Figure 1, valve V4). For each flow setting, 200 LIF images were collected and processed in order to generate average and standard deviation film thickness data, while a reading of the film surface height at each flow setting was collected using the micrometer. The aforementioned statistical values based on the LIF images were generated by randomly selecting 5 film thickness data points from each image without replacement. Once an experimental run was over (comprising approximately 10 different flow conditions spanning average film thicknesses in the 1 – 3 μm range), a second wall location measurement was conducted using the micrometer, and the two values (prior to and at the end of the run) were averaged.

This practice was adopted in order to verify that the micrometer was not displaced during an experimental run. The deviation between the initial and final wall location measurements in either of the two hereby presented independent experimental runs did not exceed 30 μm. It should finally be noted that the second experimental run was carried out by repeating the entire procedure (LIF camera and micrometer measurement calibrations). The film thickness data collected using the two measurements techniques are plotted against each other in Figure 11 (left plot).

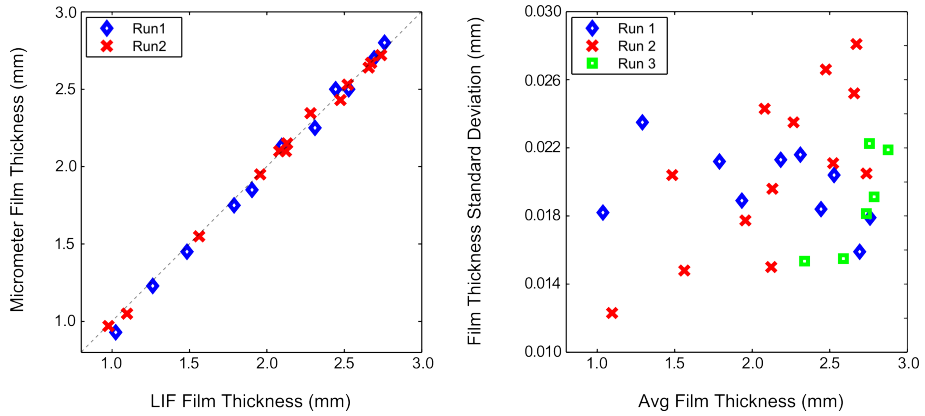


**Fig. 11** Thickness measurements of flat films carried out using a micrometer and plotted against simultaneously conducted LIF measurements (left). Quantification of the random error associated with the LIF measurements as the measurement standard deviation observed in flat films (right).

By inspection of the data presented in Figure 11, it is evident that no significant systematic error can be identified between the two measurement tactics. The span of the disparity between the micrometer and LIF-derived film thickness data is approximately 250 μm, while the average deviation between the two measurement techniques is -24 μm; the, (-) sign indicating that the LIF measurement typically overestimates the film thickness compared to the micrometer measurement. An estimate of the random error associated with the LIF-based film thickness measurement, and stemming mainly from camera noise and LIF signal scattering by PIV particles, can be obtained by looking at the film thickness standard deviation data plotted in the right plot of Figure 11 as a function of the corresponding mean film thickness values. The additional run (Run 3) data correspond to 1000 image runs carried out along with simultaneous PIV measurements. The film thickness standard deviation for all plotted data points is lower than the apparent spatial resolution (29.7 μm/pixel).

Two important parameters associated with the PIV calculation error are the particle density within the set interrogation window, and the particle image displacement. The latter is modulated by adjusting the interframe separation setting, which as was noted earlier was set to 1.ms allowing for particle displacement of around 8 – 15 pixels at the interface. However, as the fluid, and therefore the particle displacement, is a function of the location across the film, higher relative errors ensue near the wall boundary. In order to obtain a quantitative estimate of these errors, an average particle density was obtained by employment of the ImageJ image processing software package for the 32 × 32 pixel interrogation window used in the first and second passes of the PIV based vector calculation. This value corresponded to an average of 8.4 particles for the 50 images employed at $Re$ = 4.8; Keane and Adrian (Keane and Adrian 1990, Keane and Adrian 1992) showed that the probability of valid displacement detection exceeds 95% for double-frame PIV when 5 particles are present within an interrogation window of the particular size. The uncertainty in the calculated pixel displacement is 0.04 pixels for a particle image shift of at least 0.5 pixels (corresponding to 9.9 ± 0.8 mm/s).

In addition to comparisons between LIF-derived film thickness measurements and micrometer measurements, the mean film thicknesses and interfacial velocities of six flat films were compared to the 1-D, steady, fully developed flow solution of the Navier-Stokes equation, also referred to as the Nusselt solution (Nusselt 1916). The film thickness $d_{\mathrm{film}}$ prediction is expressed in Equation 9 as a function of the fluid kinematic viscosity $\nu_{\mathrm{f}}$, the flow $Re$ number, the gravitational acceleration $g$ and the inclination angle $\theta$, while the interfacial velocity $U_{\mathrm{d}}$ along the streamwise flow direction can be calculated from Equation 10:

$$d_{\text{film}} = \left(\frac{3\nu_f^2 Re}{g \sin\theta}\right)^{\frac{1}{3}} \tag{9}$$

$$U_d = \frac{g \sin\theta \, d_{\text{film}}^{\,2}}{2} \tag{10}$$

It should be noted that in the second expression, the measured rather than the predicted film thickness values were used. The calculated results are plotted against the optical measurement data in Figure 12.

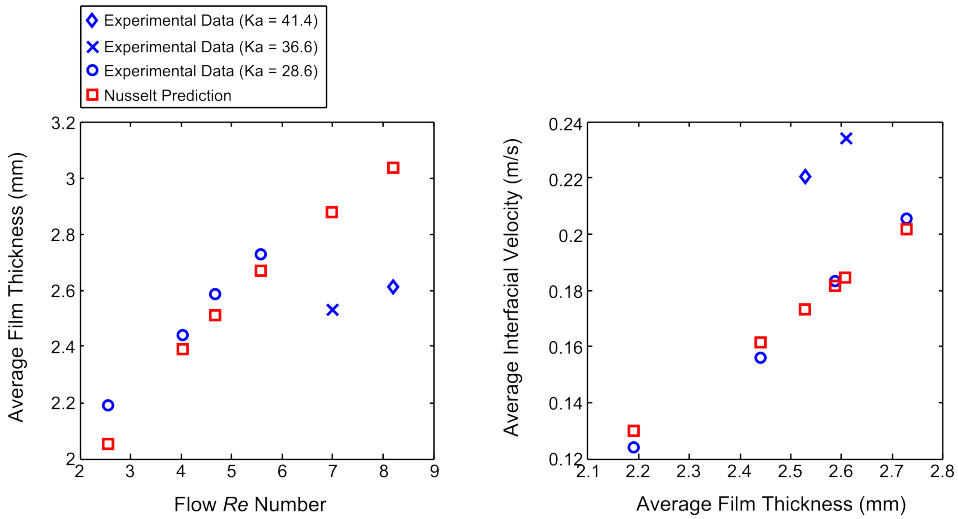


**Fig. 12** Average film thickness data obtained from LIF experiments plotted against calculated film thickness values for six different flow conditions (left). Average interfacial velocities obtained from PIV measurements, and analytically derived interfacial velocities, plotted against measured film thickness values obtained from LIF measurements for the same flow conditions (right).

By inspection of the results plotted in Figure 12, it becomes apparent that whereas the analytical calculations at $Ka$ = 28.6 match the experimental data closely, the two data pairs corresponding to $Ka$ = 36.6 and $Ka$ = 41.4 deviate substantially. The particular result is unsurprising, considering that that the relation between the surface tension and inertial forces, expressed through the $Ka$ number and representing an important parameter in the study of interfacial flows, is not captured by the analytical solution.

### 4.2 Film Topology

The purpose of this, as well as the following subsection, is to demonstrate select topological and statistical results obtained by treating raw LIF and PIV images according to the methodologies discussed in section 3. The currently implemented post-processing tactics and corresponding results are by no means exhaustive; on the contrary, they are simply indicative of the breadth of information and insight that can be gained by employment of the proposed combined optical technique. Firstly, temporal film thickness profiles are reconstructed and presented in Figure 13, with emphasis placed on the shape of the interface when the flow is subjected to different pulsation frequencies (wave frequencies). In these experiments, both the $Re$ and $Ka$ numbers were kept constant (4.8 and 28.6 respectively), while the pulsation frequency was modulated in the 1-8 Hz range by adjusting the rotational speed of the flow oscillator valve (Figure 1). In generating these profiles, a single film thickness measurement point was extracted from every instantaneous spatial film thickness profile (Figure 7). In turn, every LIF frame collected throughout an experimental run contributed one such profile. At the maximum recording rate achievable by the imagining system, 100 double frames were collected per second, yielding 200 data points; data points belonging to the same frame pair are temporarily separated by 1.5 ms, while data points originating from successive frame pairs are separated by 10 ms. Along with the plotted data points, a smoothing spline was utilized in each study-case; in the third subplot from top (corresponding to the 3 Hz wave frequency study), the data points are magnified and raised atop of the fit in order to elucidate the aforementioned practice. Regarding the observed behavior, the conducted frequency sweep can be used to demonstrate the transition from multi-peaked solitary waves to

saturated sinusoid-like waveforms as the wave frequency increases past a critical phase boundary (Liu and Gollub 1993, Liu and Gollub 1994). In more detail, two different types of non-linear forced periodic wave evolution are identified: Between 1and 3 Hz, double-peaked waveforms are observed with higher amplitude solitary waves being trailed by broader and slower, as the PIV measurements reveal, humps. Between 4 and 5 Hz, these subsidiary waveforms disappear, and only single-peaked waves are observed. It is not however until the wave frequency is increased in the 7 – 8 Hz region that waves are near sinusoidal in shape.

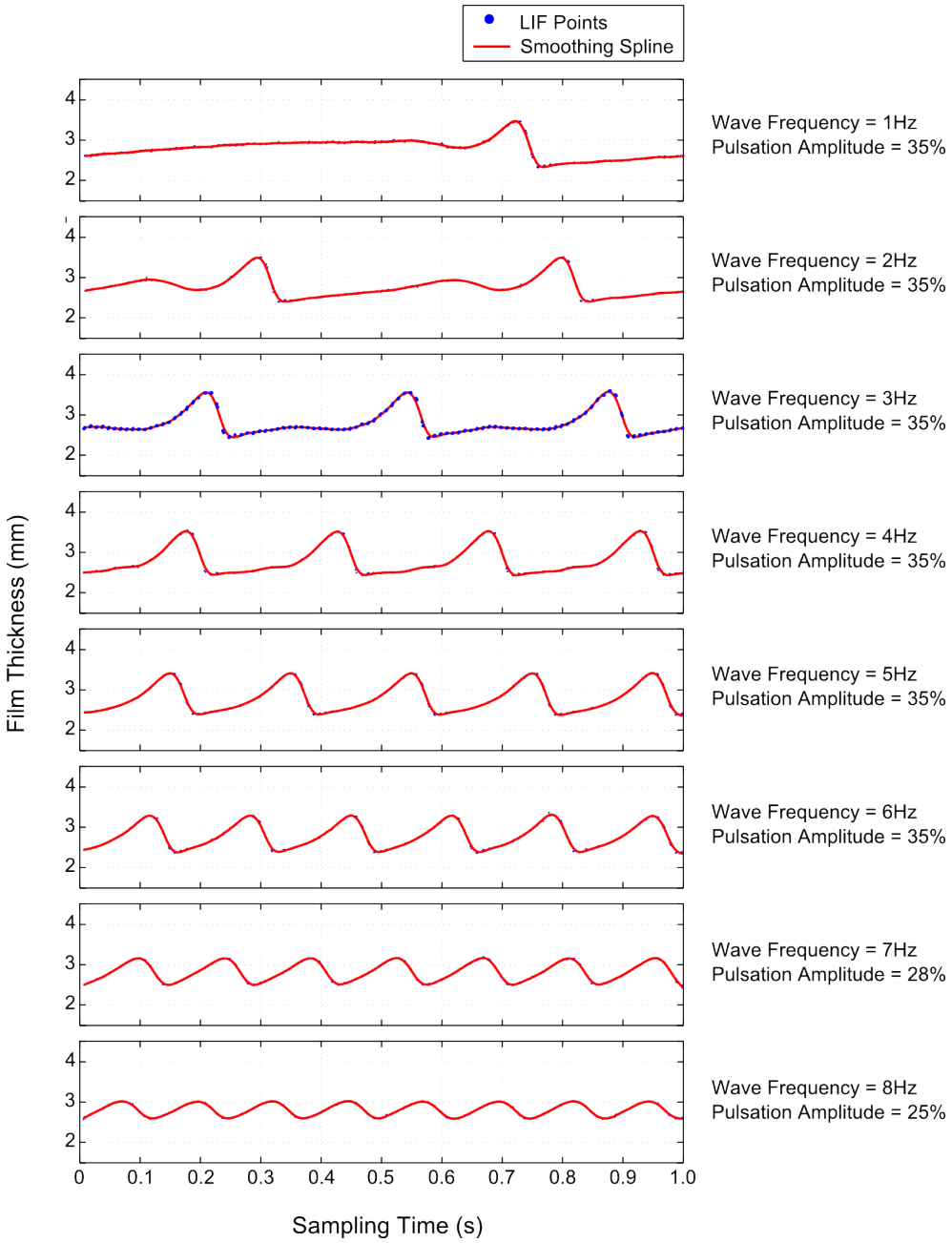


**Fig. 13** Temporal film thickness profiles generated by employment of a single film thickness measurement point (pixel) from 100 double LIF frames collected over the course of 1 s. From top to bottom, the flow pulsation frequency increases by 1 Hz, spanning the 1 – 8 Hz range. The flow *Re* and *Ka* numbers are 4.8 and 28.6 respectively.

### 4.2 Film Statistics

The observations noted earlier regarding wave topology can be verified by examining the statistics of these films and in particular the probability density functions or histograms of the observed film thickness distributions. In selecting film thickness data for the purpose of deriving statistical results, a compromise is typically reached between statistical independence and statistical convergence. Presently, statistical

quantities were derived by sampling different numbers of data from each image, uniformly at random, with and without replacement. In estimating film thickness and interfacial velocity probability density functions, the non-parametric kernel density estimation approach was employed. In Figure 14, one second film thickness and interfacial velocity time traces are plotted for $Re$ = 4.8, $Ka$ = 28.6 and wave frequency $f_w$ = 4 Hz, and $Re$ = 4.0, $Ka$ = 28.6 and wave frequency $f_w$ = 2 Hz. In estimating the interfacial velocity time traces, the same practice as discussed earlier for the film thickness time traces was employed; however, each PIV frame pair yields a single interfacial velocity value as two successive frames are required in order to generate a 2-D vector field.

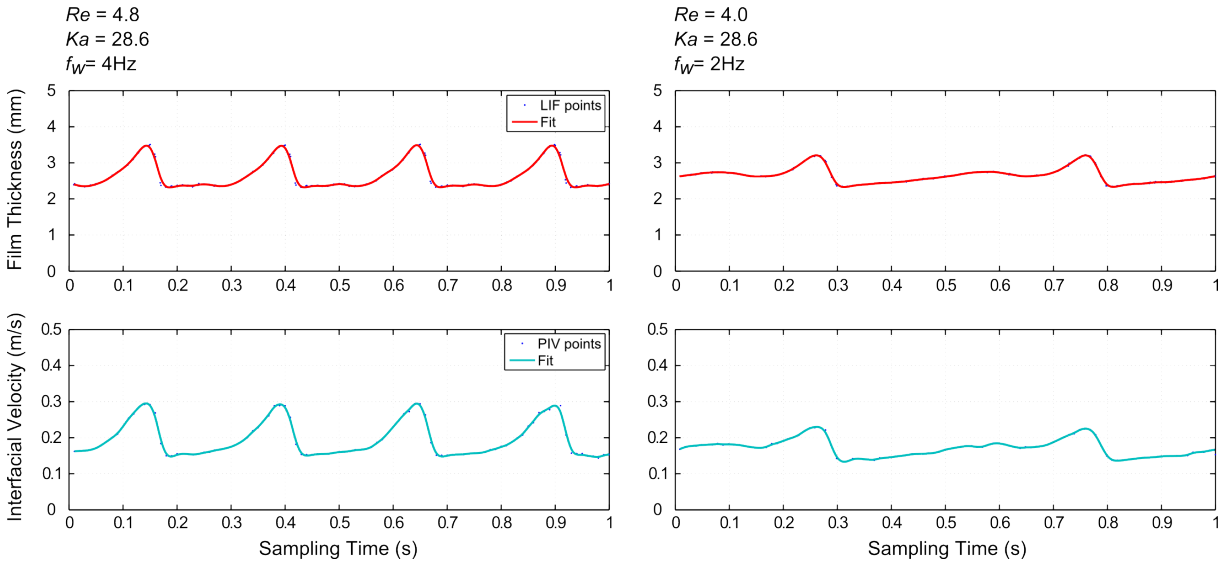


**Fig. 14** Temporal film thickness and interfacial velocity profiles produced using 100 LIF and PIV frame pairs collected over the course of 1 s. From left to right the flow conditions correspond to $Re$ = 4.8, $Ka$ = 28.6 and wave frequency $f_w$ = 4 Hz, and $Re$ = 4.0, $Ka$ = 28.6 and wave frequency $f_w$ = 2 Hz.

As expected, the topology of the thickness and velocity time traces are very similar, with wave crests displaying the highest velocities and the liquid occupying the trough regions moving slower. The double-peak profile of the 2 Hz study is also reproduced in the corresponding interfacial velocity profile, clearly suggesting that slower subsidiary waves are falling behind the faster moving solitary waves; given a longer test section, wave interactions between the primary and subsidiary peaks, such as coalesce, are believed to lead to three-dimensional instabilities and spatiotemporal chaos (Liu and Gollub 1994). It is interesting to note that despite the fact that the average thickness values of the two films are nearly identical (2.618 mm and 2.634 mm for the $f_w$ = 4 Hz and $f_w$ = 2 Hz flows, respectively), both film thickness and interfacial velocity distributions are very different. The latter are presented in Figures 15 and 16, along with histograms generated by uniformly selecting 50 sample values from each image at random and without replacement.

In Figure 15, three distinct peaks can be clearly identified in all plotted distributions; the left belonging to the through region, the middle to the subsidiary broader waves, and the right one to the faster moving solitary waves. In comparison, only two peaks can be observed in the higher frequency study case (Figure 16); one characterized by low film thickness and interfacial velocity corresponding to the through regions, and a high film thickness/interfacial velocity one corresponding to the solitary waves. In addition, the span of the $f_w$ = 4 Hz flow is wider; an indicator of the waviness of the interface, here quantified as the standard deviation in the film thickness measurement. The latter corresponds to 0.365 mm for the $f_w$ = 4 Hz flow in comparison to 0.205 mm for the $f_w$ = 2 Hz flow.

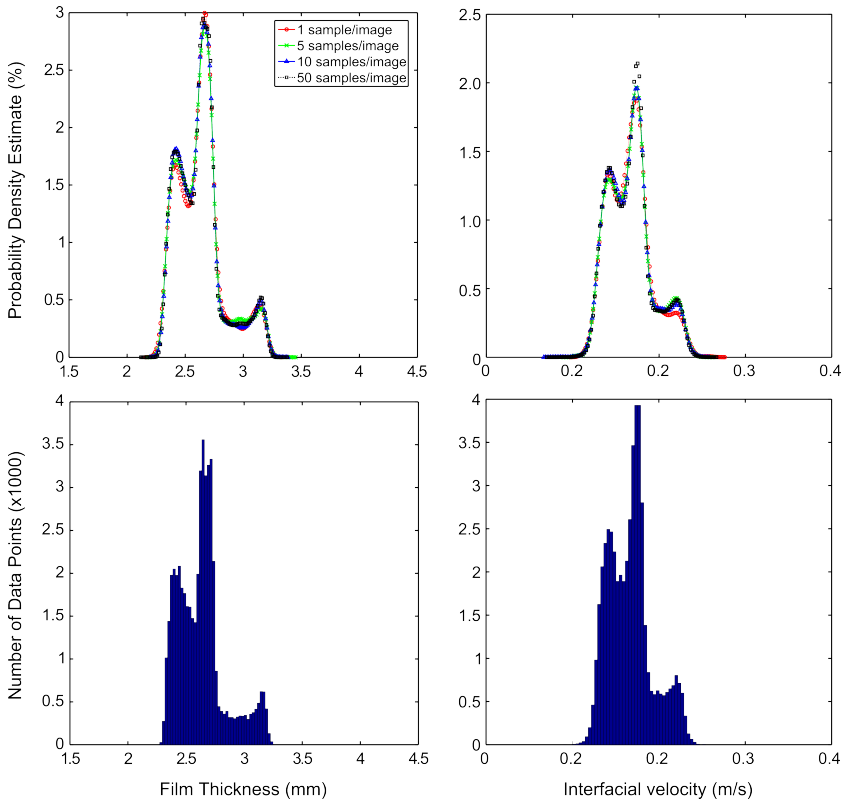


**Fig. 15** Film thickness and interfacial velocity probability density estimates generated from 1000 LIF and PIV frame pairs collected over the course of 10 s and corresponding to $Re$ = 4.8, $Ka$ = 28.6 and wave frequency $f_w$ = 2 Hz.

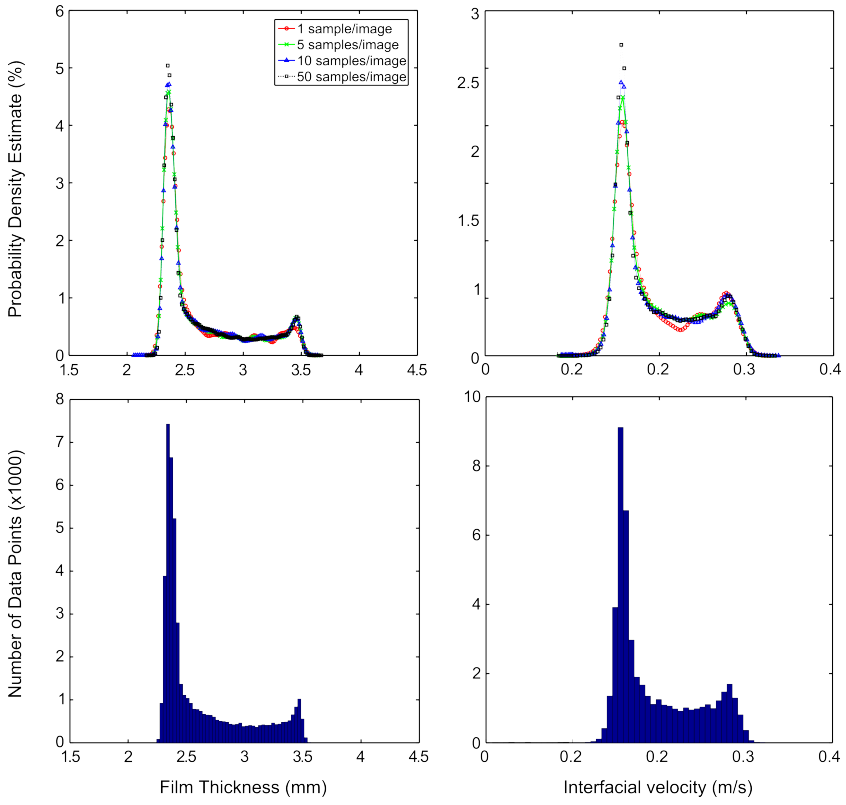


**Fig. 16** Film thickness and interfacial velocity probability density estimates generated from 1000 LIF and PIV frame pairs collected over the course of 10 s and corresponding to $Re$ = 4.8, $Ka$ = 28.6 and wave frequency $f_w$ = 4 Hz.

## 5. Conclusions

A combined optical diagnostic technique based on the simultaneous application of LIF imaging of Rhodamine-B dye and PIV/PTV using the laser light scattered from the surfaces of glass hollow spheres with mean diameter 11.7 μm, has been implemented in order to study liquid falling film flows characterized by low *Re* (2.2 – 8.2) and *Ka* (28.6 – 41.4) numbers. The experimental methodology was developed with the ultimate aim of generating local and instantaneous film thickness and interfacial velocity data, along with evaluating the velocity field from within the illuminated liquid volume inside the films, underneath the wavy free-surface of the liquid. Unlike previous film flow investigations conducted using a similar basic setup (Markides and Mathie 2013, Markides and Mathie 2013, Mathie , Nakamura and Markides 2013), modifications were introduced in order to realize an imaging of the illuminated liquid volume from the underside of the solid substrate. This particular optical arrangement offers the unique advantage of imaging the solid-liquid interface as a flat, rather than a wavy boundary. Three major challenges associated with the simultaneous implementation of the two optical diagnostic techniques were identified. The first concerned the development of a refractive index correction approach allowing for liquids with different properties (surface tension and viscosity) to be tested. The proposed solution is based on the employment of a calibration target immersed within the aqueous liquid solution, providing a scale for the optical distortion impacted upon the liquid film signal as a result of the difference in the refractive index in the optical line-of-sight. Secondly, the identification of the location of the two liquid boundaries, the solid-liquid and the gas-liquid, in the LIF images, which was addressed by employing an edge detection technique in the case of the former, and a gradient intersection approach in the case of the latter. Finally, the isolation of out-of-plane reflections from primary scattering regions in the raw PIV images was addressed by utilizing the binarized, liquid-only masks generated during the LIF image post-processing procedure.

Following a detailed account of these novel practices utilized in tackling the aforementioned challenges, the efficacy of the proposed methodology was demonstrated by comparisons between measurements conducted in flat films, film thickness measurements performed using a micrometer, and the solution to the Navier-Stokes equation, based on 1-D, steady and fully developed flow. In addition, sample film topology results were presented for a range of flow pulsation frequencies (1 – 8 Hz), while film thickness and interfacial velocity time traces were reconstructed and are presented along with statistical results of film thickness and interfacial velocity for select film flow conditions. At lower wave frequencies (1 – 3 Hz), double-peaked waveforms were observed with higher amplitude solitary waves being trailed by broader and slower waveforms. As the wave frequency was increased (4 – 5 Hz), these subsidiary waveforms disappeared and only single-peaked waves were identified. The transition from multi-peaked to single-peaked waveforms was captured by the statistical analysis, with both film thickness and interfacial velocity probability distributions displaying district triple-peaked (at 2 Hz) and double-peaked (4 Hz) shapes.

The future work associated with the study reported in the present paper includes the implementation of particle scattering signal and fluorescence emission imaging in higher *Ka* and *Re* number flows by use of lower glycerol concentrations. The particular objective entails further challenges, such as the even more restricted liquid domain (due to the lower film thickness) which will effectively limit the applicability of PIV, and the higher impact of reflections in LIF images, particularly in regions directly ahead of the main wave fronts. Regarding the data post-processing and analysis, the following objectives have been set: Along with the temporal reconstruction of the film thickness trace, a reconstruction of the wavy film interface in a spatial manner will be attempted by simultaneous employment of instantaneous thickness profile cross-correlation and interfacial velocity data available from the PIV/PTV. Using both temporal and spatial signals, power spectra will be produced with the ultimate goal of identifying the characteristic length and time scales of the investigated flows. Finally, the fact that the presently examined flows are periodic will be exploited in order to produce phased-logged averages of both the film thickness and velocity fields.

## Acknowledgements

This work was supported by the Engineering and Physical Sciences Research Council (Grant Number EP/K008595/1).

## List of References

Alekseenko, S., V. Antipin, A. Cherdantsev, S. Kharlamov and D. Markovich (2009). "Two-wave structure of liquid film and wave interrelation in annular gas-liquid flow with and without entrainment." Phys Fluids 21(6): 061701-061701-4.

Alekseenko, S., A. Cherdantsev, M. Cherdantsev, S. Isaenkov, S. Kharlamov and D. Markovich (2012). "Application of a high-speed laser-induced fluorescence technique for studying the three-dimensional structure of annular gas-liquid flow." Exp Fluids 53: 77-89.

Alekseenko, S. V., V. E. Nakoryakov and B. G. Pokusaev (1996). "Wave effect on the transfer processes in liquid films." Chem Eng Comm 141-142: 359-385.

Brauner, N. and D. M. Maron (1982). "Characteristics of inclined thin films, waviness and the associated mass transfer." Int J Heat Mass Transfer 25(1): 99-110.

Budwig, R. (1994). "Refractive index matching methods for liquid flow investigations." Exp Fluids 17(5): 350-355.

Karimi, G. and M. Kawaji (1998). "An experimental study of freely falling films in a vertical tube." Chem Eng Sci 53(20): 3501-3512

Kawaji, M. (1998). "Two-phase flow measurements using a phtochromic dye activation technique." Nucl Eng Des 184: 379-392.

Keane, R. D. and R. J. Adrian (1990). "Optimization of particle image velocimeters. I. Double pulsed systems." Meas Sci Technol 1(11): 1202-1215.

Keane, R. D. and R. J. Adrian (1992). "Theory of cross-correlation analysis of PIV images." Appl Sci Res 49(3): 191-215.

Liu, J. and J. P. Gollub (1994). "Solitary wave dynamics of film flows." Phys Fluids 6(6): 1702-1712.

Liu, L. and J. P. Gollub (1993). "Measurements of primary instabilities of film flows." J Fluid Mech 250: 69-101.

Markides, C. N. and R. Mathie (2013). Part I: A Simultaneous PLIF-IR Technique for Spatiotemporally Heat Transfer Measurements in Unsteady and Conjugate Heated Falling Film Flows. Proceedings of the 8th World Conference on Experimental Heat Transfer Fluid Mechanics and Thermodynamics, Lisbon, Portugal.

Markides, C. N. and R. Mathie (2013). Part I: Simultaneous PLIF-IR technique for Spatiotemporally resolved Heat Transfer Measurements in Unsteady and Conjugate Heated Falling Film Flows. 8th World Conference on Experimental Heat Transfer, Fluid Mechanics, and Thermodynamics Lisbon, Portugal.

Mathie, R., H. Nakamura and C. N. Markides (2013). "Heat transfer augmentation in unsteady conjugate thermal systems - Part II: Applications." Int J Heat Mass Transfer 56: 813-833.

Moran, K., J. Inumaru and M. Kawaji (2002). "Instantaneous hydrodynamics of a laminar wavy liquid film." Int. J. Multiphase Flow 28: 731-755.

Mudawar, I. and R. A. Houpt (1993). "Measurement of mass and momentum transport in wavy-laminar falling liquid films." Int J Heat Mass Transfer 37(17): 4151-4162.

Nusselt, W. (1916). "Die Oberflachenkondensation des Wasserdampfes." Z. Vereines Deutscher Ingenieure 60: 541-546.

Schagen, A., M. Modigell, G. dietze and R. Kneer (2006). "Simultaneous measurement of local film thickness and temperature distribution in wavy liquid films using a luminescence technique." Int J Heat Mass Transfer 49: 5049-5061.

Schubring, D., A. C. Ashwood, T. A. Shedd and E. T. Hurlburt (2010). "Planar laser-induced fluorescence (PLIF) measurements of liquid film thickness in annular flow. Part 1: Methods and data." Int J Multiphase Flow 36: 815-824.

Schubring, D., R. E. Foster, D. J. Rodriguez and T. A. Shedd (2009). "Two-zone analysis of wavy two-phase flow using micro-particle image velocimetry (micro-PIV)." Meas Sci Technol 20(065401).

Zadrazil, I., O. K. Matar and C. N. Markides (2014). "An experimental characterization of downwards gas-liquid annular flow by laser-induced fluorescence: Flow regimes and film statistics." Int J Multiphase Flow 60: 87-102.

Zhu, Y. M., V. Kaftandjian, G. Peix and D. Babot (1995). "Modulation transfer function evaluation of linear solid-state x-ray-sensitive detectors using edge techniques." App Opt 34(22): 4937-4943.